4-2010

Computational study of an InGaN/GaN nanocolumn light-emitting diode

Christoph Boecklin
ETH, Integrated Syst Lab

Ratko G. Veprek
ETH, Integrated Syst Lab

Sebastian Steiger
Purdue University - Main Campus, steiger@purdue.edu

Bernd Witzigmann
Univ Kassel

Boecklin, Christoph; Veprek, Ratko G.; Steiger, Sebastian; and Witzigmann, Bernd, "Computational study of an InGaN/GaN nanocolumn light-emitting diode" (2010). *Birck and NCN Publications.* Paper 634.
http://dx.doi.org/10.1103/PhysRevB.81.155306

Computational study of an InGaN/GaN nanocolumn light-emitting diode

Christoph Böcklin and Ratko G. Veprek
Integrated Systems Laboratory, ETH Zurich, Gloriastrasse 35, CH-8092 Zurich, Switzerland

Sebastian Steiger*
Network for Computational Nanotechnology, Purdue University, West Lafayette, Indiana 47907, USA

Bernd Witzigmann†
Computational Electronics and Photonics Group, University of Kassel, Wilhelmshöher Allee 71, D-34121 Kassel, Germany
(Received 29 June 2009; revised manuscript received 17 March 2010; published 6 April 2010)

A comprehensive three-dimensional analysis of the operation of an $In_{0.4}Ga_{0.6}N/GaN$ nanocolumn light-emitting diode is presented. Focus is put on the investigation of the nature and location of the emitting states. Calculations of strain and polarization-induced internal fields show that the strong lateral dependence of the potential gives rise to states confined to the periphery and to the center of the nanocolumn. However, lateral confinement of states near the column center is weak such that a quantum-well-like treatment of the remaining bound states seems appropriate where coherence is lost in the lateral directions. Within this picture, a coupled and self-consistent three-dimensional simulation of carrier transport and luminescence is presented, thus accounting for screening and lateral transport effects. Results are compared to a planar quantum-well device.

DOI: 10.1103/PhysRevB.81.155306 PACS number(s): 73.23.−b, 73.21.−b, 73.40.−c, 73.63.−b

I. INTRODUCTION

III-nitride multiquantum-well heterostructures serve as the heart of today's commerical blue and white light-emitting diodes (LEDs). In addition to many already existing applications, a substantial impact is expected over the next years on the general illumination market due to huge potential energy savings, superior color characteristics, and longevity.[1]

White LED light is usually generated by mixing the three primary colors or by down conversion of a UV source using a phosphor layer. While conventional LEDs are essentially planar structures, a novel concept is the use of nanocolumns or nanorods.[2] Growth is typically performed on Si, SiC, or sapphire substrates by either rf-plasma-assisted molecular-beam epitaxy[3,4] or metal-organic chemical vapor deposition[3] and has been reported to be almost dislocation free,[4] thus decreasing nonradiative recombination channels. Furthermore, the three-dimensional (3D) nanostructuring naturally enhances light extraction.[5] Recent progress in the position and size of nanocolumns using selective-area growth on patterned Al nucleation layers[6] allows for exceptional spatial and spectral control of these devices.

InGaN/GaN multiquantum-disk (MQD) nanocolumn LEDs, first fabricated in 2004,[7,8] have been reported to cover the entire visible emission range from blue to red.[4] The emission of conventional III-nitride devices is currently restricted to the blue and green emission range due to the highly strained active region caused by a lattice mismatch of roughly 10% between InN and GaN. Furthermore, extremely high internal fields induced by spontaneous and piezoelectric polarization give rise to a strong quantum-confined Stark effect (QCSE) and decrease the oscillator strength of the optical transition. The fact that red emission has been observed in InGaN nanocolumns may have several physical origins. Red emission would occur for mole fractions around $x=0.4$ for unstrained and $x=0.6$ in biaxially strained bulk InGaN.[9] The magnitude and lateral dependence of the indium composition has not yet been precisely determined for nanocolumns. Furthermore, lateral strain relaxation gives rise to a nontrivial three-dimensional distribution of strain and polarization.

The impact of strain and polarization on AlGaN/GaN nanocolumns has been analyzed by simulation in Refs. 10–12. Lateral relaxation greatly decreases strain near the surface. A two-dimensional (2D) analysis[12] showed that the interplay of strain-induced band-edge changes and polarization-induced fields is such that hole quantum states can be both localized near the center or near the surface, whereas electrons are always situated in the column center. As shown below, this conclusion changes in an InGaN/GaN nanocolumn.

The aim of the present work is to provide a comprehensive and quantitative three-dimensional analysis of strain, polarization, carrier localization, current flow, and luminescence in an $In_{0.4}Ga_{0.6}N/GaN$ nanocolumn. Simulations can elucidate mechanisms such as the nature and location of emitting states, screening, and lateral transport. In Sec. II a description of the simulated structure and an overview of the employed physical models are given. Section III then discusses strain, polarization, and 3D-confined quantum states. Based on these results, a three-dimensional and fully self-consistent simulation of transport and luminescence is carried out in Sec. IV.

II. MODEL

A. Structure

The considered structure resembles experimental devices investigated by Kishino *et al.*[4] A 3-nm-thick InGaN single-quantum-disk active region is sandwiched between two unintentionally p-doped (10^{17} cm^{-3}) GaN layers of 10 nm thickness, referred to later on as the intrinsic region. This heterostructure is embedded in 0.9 μm n-type (10^{18} cm^{-3})

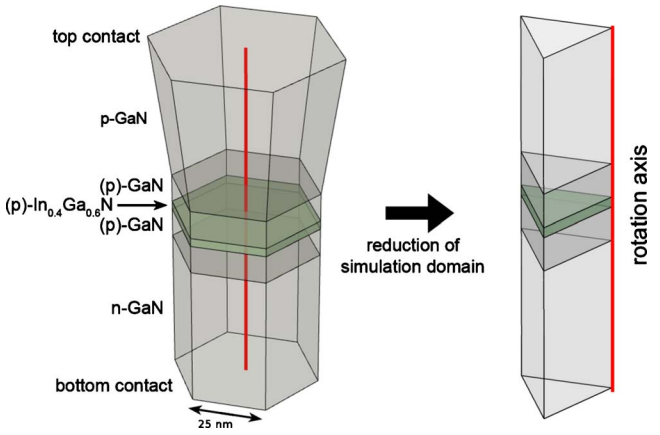

FIG. 1. (Color online) Model of an InGaN/GaN nanocolumn and reduction in the simulation domain.

GaN on the bottom and 0.6 μm p-doped (10^{18} cm^{-3}) GaN at the top. The doping values are chosen for the lack of better knowledge and complete dopant ionization is assumed.

Experimentally, the growth conditions are changed during the growth of the p layer, resulting in a gradual increase in the column diameter toward the top and a champagne-glass shape. The resulting array of columns coalesces at the top and the obtained flat and continuous top surfaces simplify the creation and contacting of the semitransparent top electrodes. In the present study, the diameter increase, which mainly results in a current spreading toward the top contact, is not modeled. By taking into account the C_6 symmetry of the column it suffices to simulate a sixth of the column (Fig. 1) which reduces computing times considerably. The radius and total height of the column are chosen to be 25 nm and $\sim$1.5 μm, respectively. A homogeneous indium distribution inside the disk is assumed for the lack of other knowledge. Growth is assumed to occur on the Ga face along the [0001] crystal direction such that the polarization-induced electric field in the quantum disk is opposite to the doping-induced built-in potential.

B. Simulation software

The optoelectronic simulation framework tdkp/AQUA (Refs. 13 and 14) developed by the authors aims at the comprehensive description of electroluminescence (EL) in multidimensional nanostructures and is employed for all simulations. tdkp (Ref. 13) calculates strain fields, polarization charges, Schrödinger states of bound particles, and luminescence spectra in quantized regions. These quantities are used in a self-consistent fashion in AQUA (Ref. 14) to solve the Poisson equation and a set of continuity equations for bound and unbound carriers to obtain the densities and the electrostatic potential throughout the structure. All calculations are performed at 300 K.

1. Strain, polarization potentials, band structure, and luminescence

The elastic strain is calculated using standard anisotropic continuum linear elasticity. The relaxed configuration of the intrinsically strained structure is obtained by minimizing the associated strain energy functional with respect to enforced boundary conditions. The resulting partial differential equations are discretized using finite elements.[15] The effect of polarization charges, caused by the variation in spontaneous and piezoelectric (strain-induced) polarization within the structure, is considered by the evaluation of volume charges on every element and surface charges on every element boundary of the computational grid. Hence, the effect of a continuous variation in strain (and possibly indium composition) and the formation of sheet charges at abrupt heterointerfaces are well represented.

Band structure calculations are carried out using a finite-element discretization of the six-band $\mathbf{k}\cdot\mathbf{p}$ envelope wurtzite Hamiltonian including strain.[16–18] This model comprises the heavy-hole, light-hole, and crystal-field split-hole valence bands (vb). The conduction band (cb) is modeled using a single band, anisotropic effective-mass Hamiltonian, as the large band gap effectively reduces the band mixing at least for the strongest bound states.

Strain, band, and polarization parameters are taken from Ref. 19, with a band offset ratio of 70:30. The polarization field is reduced to 50% of the theoretical value.[20] This choice reflects the large uncertainity regarding the application of the linear approximation of the piezoelectric effect on structures containing large amounts of lattice-mismatch induced strain.[21]

Lastly, luminescence is calculated from a standard semiclassical theory.[22] Coulomb many-body corrections are either neglected or treated on a screened Hartree-Fock level (see Sec. IV C).

2. Transport

In AQUA, the carrier density in the nanocolumn LED is partitioned into bound and unbound populations and described differently in quantized and free directions.[14] Carriers in the bulk regions are described entirely classically in all three directions. For reasons elaborated in Sec. IV, a quantum-well-like picture is adopted for carriers bound to the quantum disk which are able to move in the unbound (transverse) directions by drift and diffusion but retain their coherence and quantum-mechanical wave function in the confined direction (growth direction).

This partitioning leads to a system of coupled transport equations for populations defined on grids with varying dimensionality: two 3D continuity equations for the unbound populations $n_{3D}(x_{3D})$, $p_{3D}(x_{3D})$, two 2D continuity equations for the bound populations $n_{2D}(x_{2D})$ and $p_{2D}(x_{2D})$, and the 3D Poisson equation for the electrostatic potential $\phi(x_{3D})$. x_{3D} and x_{2D} here denote the coordinates within the different grids. The band edge governing movement of the 3D populations is corrected in the quantum region because such carriers cannot have energies below the barrier band edges. The heterointerface is instead modeled by the possible capture into the energetically lower population.

The description of bound carriers in the quantized direction requires the solution of a Schrödinger equation in the quantized direction at a selection of 54 different lateral positions within the quantum disk, termed $\mathbf{k}\cdot\mathbf{p}$ slices[14] (Fig. 2).

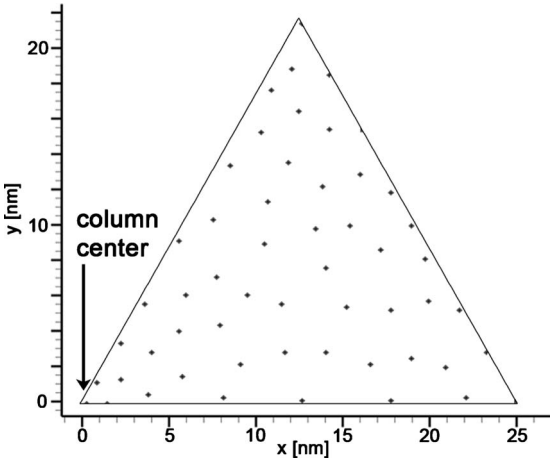

FIG. 2. Locations where one-dimensional $\mathbf{k}\cdot\mathbf{p}$ luminescence calculations are carried out ($\mathbf{k}\cdot\mathbf{p}$ slices).

The spreading shape and luminescence are linearly interpolated in between.

The exchange of carriers between populations is mediated by a capture mechanism, acting as a recombination term for the unbound population and as a generation term for the bound population, using a capture time of 10^{-12} s. Arora mobility parameters are taken from Ref. 19. Further parameters include a Shockley-Read-Hall (SRH) recombination time of 2×10^{-8} s, reflecting the reduced dislocation density in nanocolumns, and an Auger coefficient of 10^{-31} s. Both parameters are not well established in the literature. The 3D grid for the transport of unbound carriers, 2D grid for the transport of bound carriers, and one-dimensional (1D) grid for the wave function of bound carriers contain 15 400, 8500, and 290 vertices, respectively. Surface effects such as Fermi-level pinning are not taken into account in the simulations.

III. STRAIN, POLARIZATION POTENTIALS, AND CARRIER CONFINEMENT

A fundamental question in the description of lateral transport in the active layer of nanocolumns is whether a classical drift and diffusion or a coherent quantum-mechanical picture is adequate. While the strong confinement leads to coherence in the growth direction, the lateral extension of the nanocolumn is rather large and therefore suggests that carriers scatter and lose coherence. As a result, an incoherent description of lateral transport would be suitable. Due to the inhomogeneous strain relaxation, as shown below, such a quantum-well-like picture cannot be justified without further arguments, as the inhomogeneity of the band edges possibly gives rise to the formation of quantum-dotlike states. The present section aims to revisit the strain relaxation and resulting polarization fields[9] and then presents 3D $\mathbf{k}\cdot\mathbf{p}$ calculations of conduction band and valence band states to investigate lateral confinement. Furthermore, interband transition rates are analyzed to gain information on the relevance of the states for optical transitions. The doped regions at the top and bottom of the nanocolumn are excluded for the $\mathbf{k}\cdot\mathbf{p}$ calculations.

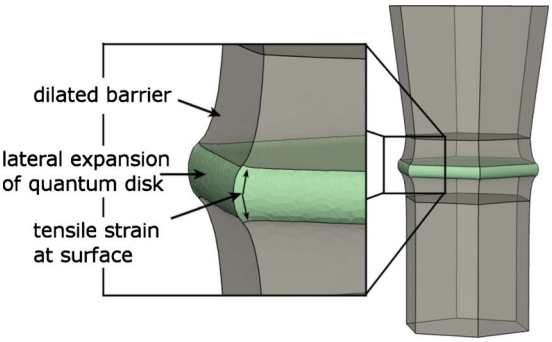

FIG. 3. (Color online) Displacement of the relaxed single-quantum-disk structure, magnified by a factor of 10.

A. Intrinsic strain relaxation and polarization potential

The finite diameter of the nanocolumn allows, in contrast to planar structures, for a fully three-dimensional relaxation of the strains.[9,10] As a consequence, the heavily strained quantum disk does not only relax by Poisson's ratio in the growth direction but experiences a significant lateral extension. This situation is shown in Fig. 3, where the resulting displacement of the relaxation has been scaled by a factor of 10 for illustrative purposes. The lateral expansion of the quantum disk even leads to dilatation toward and at the nanocolumn surface, significantly lowering the bulk bandgap in that area. In the center of the nanocolumn, the strains approach the biaxial limit. Besides relaxation in the quantum disk, the lateral extension causes tensile strains within the barriers while in planar structures the barriers remain unstrained.

The resulting bulk band edges for the conduction and valence bands including strain effects within the quantum-disk active region are depicted in Fig. 4. The band edges are heavily distorted. The difference between the maximal and

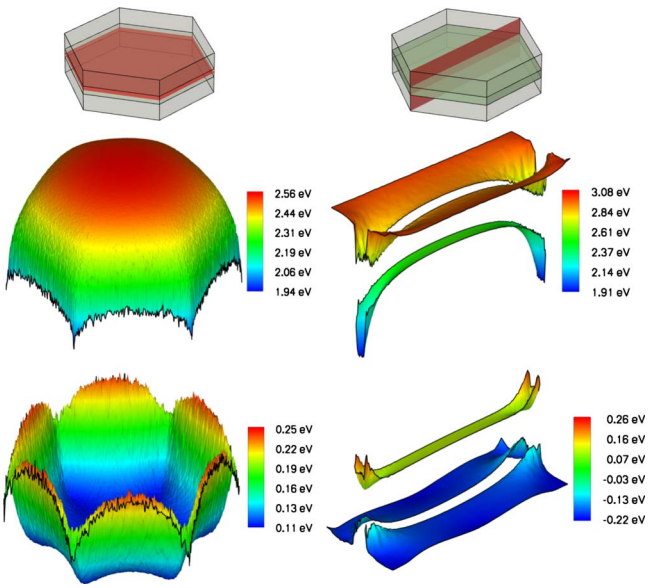

FIG. 4. (Color online) Band edges with the strain effect taken into account. The jittered boundaries in the left graphs are due to meshing and visualization effects.

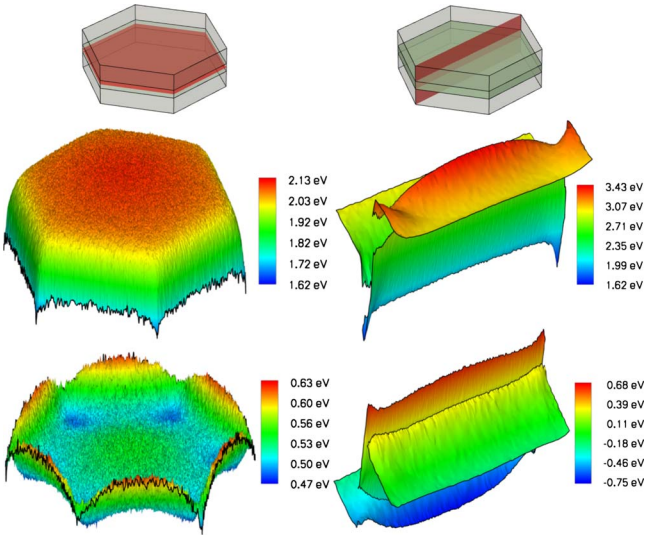

FIG. 5. (Color online) Band edges with polarization and strain effects taken into account. For the conduction band, the strain effect is dominant (confinement at the edges), whereas for the valence band, the polarization potential is dominant for low-energy states (confinement at the center).

minimal values is as much as 630 meV for the conduction band edge and 160 meV for the valence band edge. Hence, the strain tends to confine the strongest bound carriers at the corners (electrons) or edges (holes) of the nanocolumn.

A central consequence of the inhomogeneous strain relaxation and finite diameter of the nanocolumn is a pronounced inhomogeneous distribution of polarization charges and therefore a significant variation in the polarization potential, i.e., the electrostatic potential induced by the polarization charges. Another source of difference is the fact that electric field lines are able to pass through the surrounding air. As a result, the polarization potential is lowered toward the surface and tends to confine the carriers in the middle of the structure. Adding the polarization potential, the resulting band edges are depicted in Fig. 5. While the strain tends to confine carriers toward the surface, the polarization potential favors a confinement in the middle of the structure and therefore, the dominating effect must be assessed using a quantitative 3D Schrödinger calculation.

B. 3D k·p states, transition matrix elements

The 3D Schrödinger calculation is performed using the $\mathbf{k}\cdot\mathbf{p}$ 6×6 method[13,16,18] for the valence bands and the single-band anisotropic effective-mass model for the conduction band on a 700 000 vertex grid of the active layer, the intrinsic barriers, and the surrounding air. The calculations are performed without an applied external potential (i.e., flat band) except for the polarization potential. The boundary conditions for Poisson's equation are set such that the potential is zero at the top and the bottom of the structure while on the remaining surfaces zero-field conditions are enforced. The isoprobability surfaces of the wave functions are shown for the first states in the cb and vb for the case where only strain is considered (Fig. 6) and when including both the strain and the polarization potential (Fig. 7). The energies corresponding to these states are given in Table I. Figure 6 reveals that the strain field indeed leads to a strong localization of the states toward the surface. While cb states are localized in the corners, vb states tend to be located in the middle of the surfaces. Including the polarization potential drastically changes this finding. As shown in Fig. 7, the first cb states are still located in the corners, near the surface, while the first vb states now lie near the nanocolumn center.

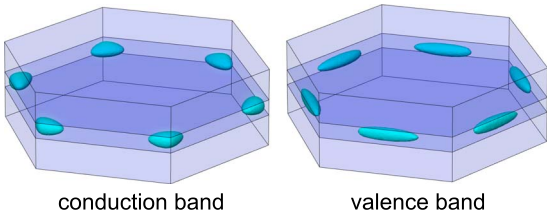

FIG. 6. (Color online) Isoprobability surfaces of the first conduction band (left) and valence band (right) states in the strained quantum disk. The quantum disk is given by the darker blue (darker gray) area in the middle of the structure, surrounded by the light blue (light gray) intrinsic GaN layer.

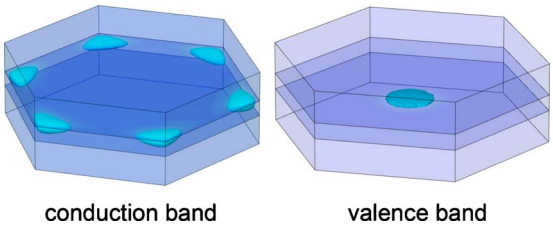

FIG. 7. (Color online) Isoprobability surfaces of the first conduction band and valence band states considering strain and polarization potential in the quantum disk.

While these arguments focus on the lowest states, a more complete picture of the nature of bound carriers can be deduced from the density of states. In order to obtain a measure from the discrete energies of a 3D calculation, simulations are performed to find the first 320 cb and 240 vb eigenstates and corresponding eigenenergies. The number of valence band states is intentionally reduced to lower the computational burden induced by the $\mathbf{k}\cdot\mathbf{p}$ 6×6 valence band model. The energy levels are then converted to Lorentzians with full widths at half maximum (FWHMs) of 2 meV for the vb and 10 meV for the cb and summed up for visualization purposes. The single Lorentizans are normalized such that their peak equals 1, allowing to determine the degeneracy of isolated states from the resulting plots. Strongly confined states are expected to be clearly separated from the continuum in the resulting figure while the formation of a 2D-like density

TABLE I. Energies of the states depicted in Figs. 6 and 7. The given degeneracy excludes spin.

	First state (eV)	Degeneracy	Next state (eV)
cb (strain only)	2.483	6	2.522
vb (strain only)	0.121	6	0.105
cb (polarization and strain)	2.342	6	2.356
vb (polarization and strain)	0.391	1	0.387

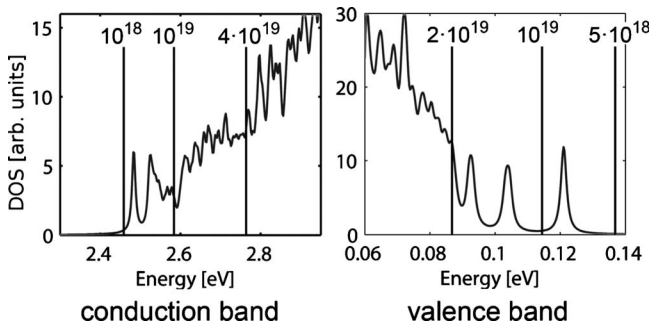

FIG. 8. Density of states of the strained quantum disk. The vertical black lines denote the location of the corresponding Fermi levels at 300 K for different 3D carrier densities (in cm^{-3}).

of states hints that a quantum-well picture is more appropriate.

The density of states for the calculation including only the strain, shown in Fig. 8, exhibits discrete peaks clearly separated from the continuum. These peaks can be attributed to the first (sixfold degenerate) states. Such states would call for a quantum-dotlike treatment of the active region. Figure 9 shows the density of states for the calculation including strain and polarization fields. The first peak of the sixfold degenerate cb states is still visible but the clear separation from the continuum disappears. Moreover, in the density of states of the valence band, the separation from the continuum vanishes completely.

In addition, the energetic separation between states, which can be termed localized and nonlocalized states, is only on the order of a few meV. Given that large carrier densities are present in the active zone of light-emitting diodes and operation takes place at room temperature, scattering between these states should be large and significant coherence loss is expected to occur.

An important observation is that while the bulk band edges in Figs. 4 and 5 show very low band-edge energies in the vicinity of the surface, lateral quantization effects lead to the fact that no particle can occupy such low energies (see also the onset of the band structure in Figs. 8 and 9). This lateral quantization energy must be included when calculating emission spectra, a point to which we will return in the next section.

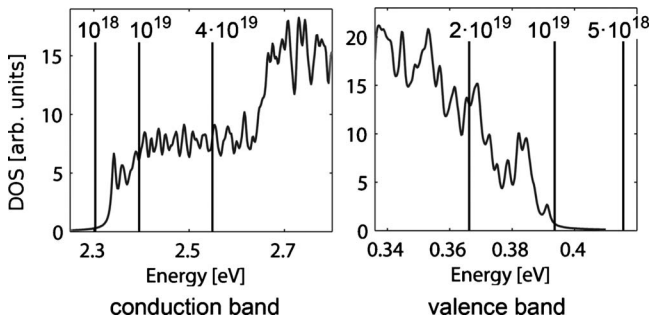

FIG. 9. Density of states of the quantum disk considering strain and polarization potential. The black lines denote the location of the corresponding Fermi levels at 300 K for different 3D carrier densities (in cm^{-3}).

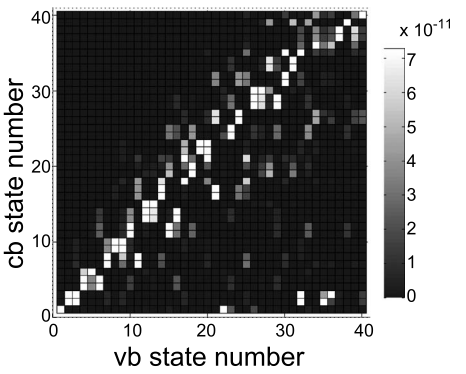

FIG. 10. Transition strengths (in kg eV) between the lowest 40 (80 doubly degenerate) valence- and conduction band states, assuming an unstrained system and excluding the polarization potential.

In Figs. 10 and 11, the optical transition matrix elements are shown for transitions between the first 40 cb and vb states. The matrix elements of the three polarization directions are averaged (i.e., $p_{\mathrm{tot}}=\frac{1}{3}\Sigma_i p_i$, where $i=x$, y, and z, and p_i is the matrix element in a certain direction) and both spin orientations are summed together. Figure 10 shows the calculation ignoring strain and polarization potentials while for Fig. 11, these effects are included. The transition matrix elements in Fig. 10 are predominantly diagonal, corresponding to the usual in-plane momentum conservation of direct transitions. In contrast, the transition matrix elements in Fig. 11 reveal a complex picture reflecting the localization of the states in an inhomogeneous system. vb states 3–11 are located near the periphery and hence exhibit a rather large overlap with the first 12 cb states, which are predominantly localized near the surface. However, above state number 20 localization can also take place near the column center. When including 100% instead of 50% of the polarization potential with parameters from Ref. 19, all the valence band states are located near the center and consequently, the first 16 states are optically dark. Comparing the magnitudes in Figs. 10 and 11, the transition strengths are lowered significantly by the strain and polarization effects. Screening and the applied voltage will partly compensate for this at operating conditions.

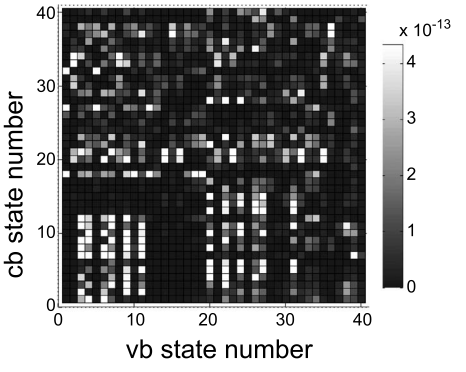

FIG. 11. Transition strengths (in kg eV) between the lowest 40 (80 doubly degenerate) valence- and conduction band states of the strained system including the polarization potential.

IV. TRANSPORT AND ELECTROLUMINESCENCE

The preceding section showed that the localization of emitting 3D states is very sensitive to the assumed parameter sets and a mixture of states near the center and states near the periphery is expected to take part in the luminescence. Several aspects need to be considered in this regard. First, the presented 3D states are valid for empty bands and the potential landscape will be altered when populating them. In fact, the potential induced by the space charge of just a single 3D state can be as large as tens of millielectron volt. Second, the inhomogeneous transition rates in Fig. 11 suggest a complicated mixture of emitting states, even more so when considering the fact that population of such states happens through capture of unbound carriers, which is likely to populate excited states first. Third, the absence of energetic separation suggests large scattering rates and associated decoherence.

It is not clear how electroluminescence, i.e., luminescence coupled to carrier transport with injection from electrical contacts, can be modeled taking into account these complex three-dimensional dependencies. In an attempt to retain a physically meaningful yet feasible transport model, a picture is adopted in which bound carriers are described by their wave function in the growth direction, where confinement is strong for all bound states but which behave classically in the lateral directions, movement being governed by drift and diffusion. However, such an approach must still take into account the lateral quantization energy especially for carriers located near the periphery.

A. Lateral drift-diffusion potential, correction of emission spectrum

Due to the different locations in growth direction, lateral movement of electrons and holes is expected to occur in different planes and to be influenced by the polarization-induced potential which vanishes by symmetry in the exact middle of the quantum disk. Moreover, it would be ill advised to include the steep fall of the band edges toward the surface in a drift-diffusion picture because lateral quantization effects prohibit such low energies. The question of the correct lateral potential governing the movement is therefore nontrivial.

The following attempt tries to account for these effects. Lateral drift and diffusion happen with the band edges shown in Fig. 12, where the fall toward the surface is cut off and the polarization-induced potential is taken 1.25 nm above (electrons) and below (holes) the disk center. These locations are roughly the center-of-mass positions of the carrier wave functions in the vertical direction. The potential arising from the carrier system adds to the shown potential but is comparatively small because no significant lateral separation between electrons and holes occurs in the lateral drift-diffusion picture. The cutoff is determined by a 2D Schrödinger calculation determining the lowest bound electron and hole levels. The difference between the cutoff and the bulk band edge at a $\mathbf{k}\cdot\mathbf{p}$ slice approximates the lateral quantization energy and the emission spectrum from that slice is shifted by this amount.

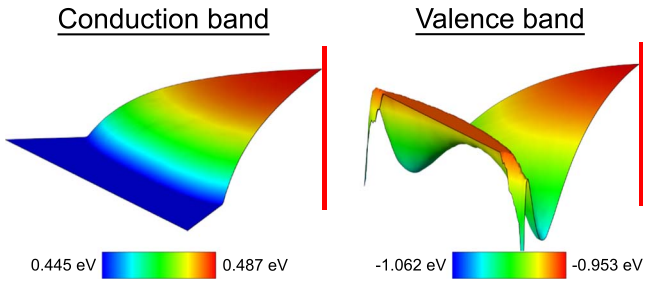

FIG. 12. (Color online) Lateral dependence of the conduction and valence bands whose gradients contribute to the drift-diffusion equations of confined carriers. Strain and polarization are included 1.25 nm above (electrons) and below (holes) the disk center and cutoff near the surface. The vertical red (gray) line indicates the lateral center of the disk. Note that the energy zero is different in this plot compared to Fig. 5.

B. Microscopic results near turn-on

Defining a turn-on point at 5 $\mathrm{A/cm^2}$ or 3.1 V (Fig. 15), the spatially resolved radiative recombination at this voltage is shown in Fig. 13. A slight numerical asymmetry is present due to the large number of interpolations, finite grid sizes, and a finite number of $\mathbf{k}\cdot\mathbf{p}$ slices.[14] Emission mainly arises from the periphery. The lack of lateral separation between electrons and holes results in a low space charge and therefore the lateral dependency of the band edges at turn-on is similar to the zero-density situation shown in Fig. 12.

Carriers actually first reach the column periphery, as is apparent from the 3D current density depicted in Fig. 14(a). The plot displays the drift-diffusion current densities of the unbound electrons (blue, negative scale) and holes (yellow/red, positive scale). Only the magnitudes are shown as tdkp/AQUA is currently not able to generate plots of vectorial fields. In our model, incident unbound carriers are drawn to the surface by the nonuniform polarization-induced potential. The strain-dependent band-edge shift, which is not taken into account for the 3D carriers, would further enhance this effect. The reduced barrier near the column surface, shown in Fig. 14(b), facilitates current flow. Carriers entering the quantum disk are then captured and transferred to the 2D population as they flow toward the axial center of the column.

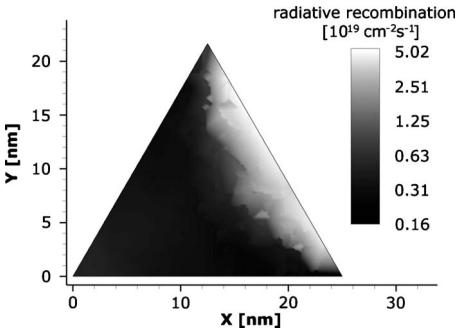

FIG. 13. Lateral dependence of the radiative recombination in logarithmic scale in the quantum disk at turn-on of 3.1 V. The nanocolumn center is at (0,0). The recombination is predominantely located at the periphery.

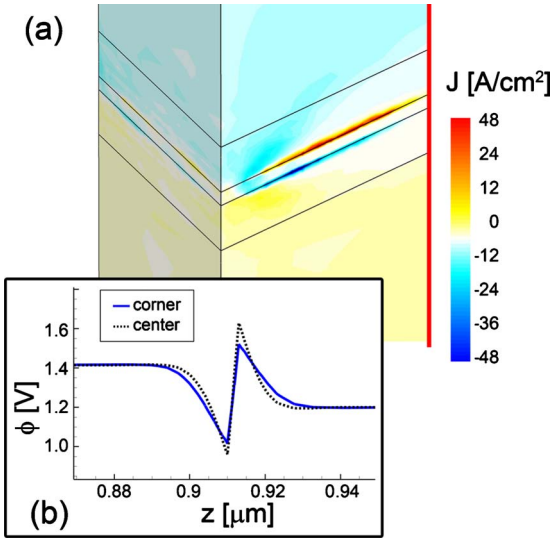

FIG. 14. (Color online) (a) Magnitudes of the electron (blue) and hole (yellow/red) electrical current densities at turn-on. The red (gray) line depicts the column center. (b) Dependence of the band edges governing 3D carrier motion in the growth direction at the center and near a corner of the hexagonal column. Unbound carriers experience no more heterointerface jumps (see Sec. II B), the presence of the quantum disk is mainly reflected in the polarization-induced potential and the presence of capture into the confined population.

C. *I-V* and *P-V* characteristics, emission spectra

The simulated *I-V* and *P-V* curves, shown in Fig. 15, exhibit the approximate exponential characteristics common to all LED structures. Due to an increasing internal quantum efficiency (IQE) at moderate and high voltages, output power increases faster than current. At even higher voltages, Auger recombination and electron leakage become more important and the IQE drops again (efficiency droop). Leakage does not play a role at the presented voltages.

For comparison, a planar single-quantum-well LED with the same material composition and doping profile was simulated, although the indium content in the active layer is too large to be experimentally realized. The results, also shown in Fig. 15, are shifted to higher voltages because the reduced polarization barrier of the nanocolumn facilitates current flow.

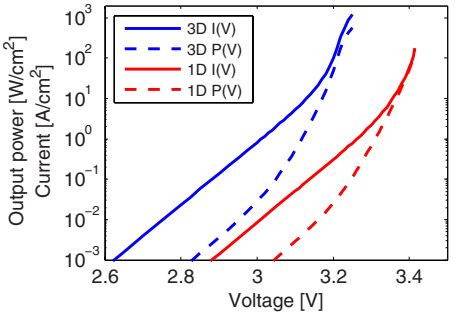

FIG. 15. (Color online) *I-V* (solid) and *P-V* (dashed) characteristics of the nanocolumn LED (labeled "3D") and a similar planar device (labeled "1D").

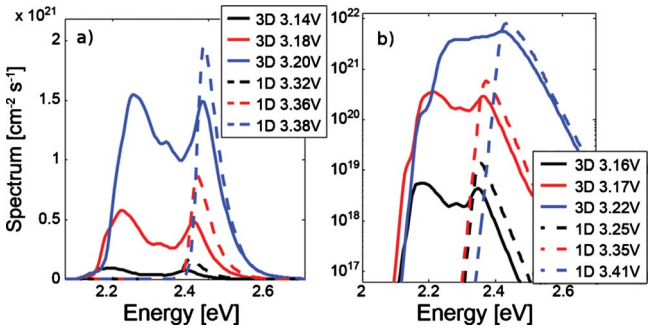

FIG. 16. (Color online) Emission spectra in the nanocolumn LED (solid, labeled "3D") and in a similar planar device (dashed, labeled "1D"). (a) is in linear scale and (b) logarithmic scale.

In Fig. 16, EL emission spectra of the nanocolumn are plotted both on a linear and on a logarithmic scale along with results for the planar quantum well. Generally the nanocolumn spectra are broader (with a FWHM of roughly 200 meV compared to 50 meV for the 1D device). The broadening originates from emission from different locations inside the quantum disk, the low-energy side stemming from the peripheral region. A blueshift of up to 50 meV is observed at high voltages for both the nanocolumn and the planar LED. The blueshift is caused by the increased screening of the polarization charges, reducing the QCSE. The blueshift starts at lower current densities in the nanocolumn LED because the density is concentrated near the column center.

V. DISCUSSION

The presented simulation results suggest that emission at low and moderate voltages arises from the column periphery. It must be noted that this conclusion is very sensitive to the assumed parameters for the polarization potential. Including 100% instead of 50% of the values in Ref. 19 leads to drift-diffusion band edges which are lowered toward the center and consequently the main emission arises from the center where the biaxial strain value is approached. The analysis of Ref. 23, where photoluminescence (PL) in InGaN/GaN MQD nanocolumns including emission rates and blueshifts and their dependency on the column diameter was investigated, concludes that transition matrix elements between 1D states near the surface are enhanced due to strain relaxation and hence emission is also likely to occur from the region close to the surface. However, the transport model differs considerably from the present model in that it is one dimensional, leading to a laterally uniform carrier density and in that carriers are generated by optical generation. In our case emission arises from the periphery due to higher carrier densities rather than enhanced emission rates. Experiments comparing EL and PL measurements of the same sample could shed more light on the spatial location of the emission.

An important issue in the calculation of emission energies is the influence of Coulomb many-body corrections which induce a density-dependent renormalization of the band edges and emission spectra.[22] The spectra in Fig. 16 are calculated in the absence of these corrections. However, due to

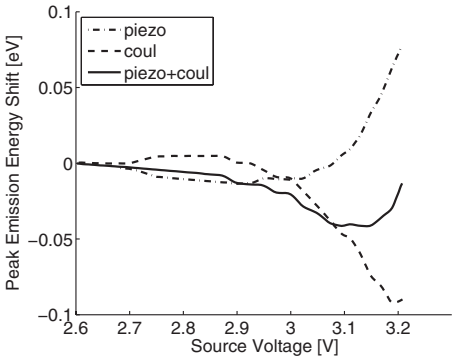

FIG. 17. Shifts of the peak emission energy due to screening of polarization charges (dashed dotted), Coulomb renormalization (dashed), and both effects together (solid) for the nanocolumn LED. The two effects lead to shifts of opposite sign, partially canceling each other.

the relatively low static dielectric constant in nitride materials (wz-GaN: ϵ_r=9.5–10.4 depending on the crystal direction and zb-GaAs: ϵ_r=12.9), the effect is expected to be important.[24] An *a posteriori* calculation of the redshift due to carrier-carrier interactions on the screened Hartree-Fock theory level and using the same densities as in Sec. IV is depicted in Fig. 17, showing that the magnitude roughly equals the screening-induced blueshift. This canceling effect possibly explains why no blueshift has been observed experimentally in micro-EL experiments.[4] The large blueshift observed when probing the whole sample may result from different mole fractions and thus different polarization-induced potential barriers [Fig. 14(b)], turn-on voltages and emission peaks for individual columns, all of which are connected in parallel. It should be noted that Coulomb renormalization dominates over screening at lower indium contents because the renormalization is not as sensitive to a change in mole fraction as the internal field.

In the present analysis, the experimentally observed variation in emission wavelengths from red to blue[4] is explained by large mole fraction variations. However, there is significant experimental uncertainty about the exact material composition, indium homogeneity and maybe even crystal orientation within the active region. Considering the recent advances in the growth control, further experimental data will shed more light on these issues.

VI. CONCLUSION

This paper presents a self-consistent three-dimensional computational study of an InGaN-GaN nanocolumn covering the most relevant physical effects such as strain, polarization potentials, quantum confinement, carrier transport, and luminescence. Strain relaxation leads to a complicated mixture of states confined to the periphery and to the center of the column. Since the energetic separation between these states is small and scattering is large, a quantum-well-like picture is adopted for the calculation of electroluminescence. Injected bulk carriers get drawn toward the column periphery due to the inhomogeneous strain and polarization potentials, and emission is dominated by carriers near the periphery. However, the fragile interplay between strain and polarization makes this conclusion sensitive to the assumed parameter sets. The obtained emission spectra are redshifted and broader compared to planar devices. Further experiments comparing PL and EL measurements as well as diameter variations in EL measurements and determinations of the exact material composition are needed to further elucidate the microscopic origins of the emission.

ACKNOWLEDGMENT

This work was funded through Grant No. 200021-107932 of the Swiss National Science Foundation (SNSF).

*steiger@purdue.edu
†bernd.witzigmann@uni-kassel.de

[1] M. R. Krames, O. B. Shchekin, R. Mueller-Mach, G. O. Mueller, L. Zhou, G. Harbers, and M. G. Crawford, J. Disp. Technol. **3**, 160 (2007).
[2] M. Yoshizawa, A. Kikuchi, M. Mori, N. Fujita, and K. Kishino, Jpn. J. Appl. Phys., Part 2 **36**, L459 (1997).
[3] A. Kikuchi, M. Tada, K. Miwa, and K. Kishino, Proc. SPIE **6129**, 612905 (2006).
[4] K. Kishino, A. Kikuchi, H. Sekiguchi, and S. Ishizawa, Proc. SPIE **6473**, 64730T (2007).
[5] H. W. Choi, M. D. Dawson, P. R. Edwards, and R. W. Martin, Appl. Phys. Lett. **83**, 4483 (2003).
[6] K. Kishino, H. Sekiguchi, and A. Kikuchi, J. Cryst. Growth **311**, 2063 (2009).
[7] H.-M. Kim, Y.-H. Cho, H. Lee, S. I. Kim, S. R. Ryu, D. Y. Kim, T. W. Kang, and K. S. Chung, Nano Lett. **4**, 1059 (2004).
[8] A. Kikuchi, M. Kawai, M. Tada, and K. Kishino, Jpn. J. Appl. Phys., Part 2 **43**, L1524 (2004).
[9] R. G. Veprek, S. Steiger, and B. Witzigmann, Phys. Status Solidi C **6**, S506 (2009).
[10] M. Povolotskyi and A. Di Carlo, J. Appl. Phys. **100**, 063514 (2006).
[11] J. Ristić, C. Rivera, E. Calleja, S. Fernández-Garrido, M. Povoloskyi, and A. Di Carlo, Phys. Rev. B **72**, 085330 (2005).
[12] C. Rivera, U. Jahn, T. Flissikowski, J. L. Pau, E. Munoz, and H. T. Grahn, Phys. Rev. B **75**, 045316 (2007).
[13] R. G. Veprek, S. Steiger, and B. Witzigmann, J. Comput. Electron. **7**, 521 (2008).
[14] S. Steiger, R. G. Veprek, and B. Witzigmann, J. Comput. Electron. **7**, 509 (2008).
[15] D. Braess, *Finite Elemente* (Springer, Berlin, 1997).
[16] S. L. Chuang and C. S. Chang, Phys. Rev. B **54**, 2491 (1996).
[17] R. G. Veprek, S. Steiger, and B. Witzigmann, Phys. Rev. B **76**, 165320 (2007).
[18] R. G. Veprek, S. Steiger, and B. Witzigmann, Opt. Quantum Electron. **40**, 1169 (2008).
[19] J. Piprek, *Nitride Semiconductor Devices: Principles and Simu-*

lation (Wiley, New York, 2007).
[20] M.-C. Tsai, S.-H. Yen, S.-H. Chang, and Y.-K. Kuo, Opt. Commun. **282**, 1589 (2009).
[21] G. Bester, X. Wu, D. Vanderbilt, and A. Zunger, Phys. Rev. Lett. **96**, 187602 (2006).
[22] W. W. Chow and S. W. Koch, *Semiconductor—Laser Fundamentals* (Springer, Berlin, 1999).
[23] Y.-R. Wu, C. Chiu, C.-Y. Chang, P. Yu, and H.-C. Kuo, IEEE J. Sel. Top. Quantum Electron. **15**, 1226 (2009).
[24] H. Haug and S. W. Koch, *Quantum Theory of the Optical and Electronic Properties of Semiconductors* (World Scientific, Singapore, 2004).